



## Microstructural study of multiaxial low cycle fatigue

Masao Sakane, Takamoto Itoh

*Ritsumeikan University, Department of Mechanical Engineering, 1-1-1 Nojibigashi, Kusatsu, Shiga, 525-8577, Japan*  
*sakanem@se.ritsumei.ac.jp, itohataka@fc.ritsumei.ac.jp*

**ABSTRACT.** This paper discusses the relationship between the stress response and the microstructure under tension-torsion multiaxial proportional and nonproportional loadings. Firstly, this paper discusses the material dependency of additional hardening of FCC materials in relation with the stacking fault energy of the materials. The FCC materials studied were Type 304 stainless steel, pure copper, pure nickel, pure aluminum and 6061 aluminum alloy. The material with lower stacking fault energy showed stronger additional hardening, which was discussed in relation with slip morphology and dislocation structures. This paper, next, discusses dislocation structures of Type 304 stainless steel under proportional and nonproportional loadings at high temperature. The relationship between the microstructure and the hardening behavior whether isotropic or anisotropic was discussed. The re-arrangeability of dislocation structure was discussed in loading mode change tests. Microstructures of the steel was discussed in more extensively programmed multiaxial low cycle fatigue tests at room temperature, where three microstructures, dislocation bundle, stacking fault and cells, which were discussed in relation with the stress response. Finally, temperature dependence of the microstructure was discussed under proportional and nonproportional loadings, by comparing the microstructures observed at room and high temperatures.

**KEYWORDS.** Multiaxial fatigue; Microstructure; Stainless steel; Dislocation; Stacking fault energy; Twin

### INTRODUCTION

Multiaxial low cycle fatigue (LCF) is one of the key issues for appropriate designs and safe operations of machines since some of machines undergo multiaxial LCF damage. Stress parameters have been widely used to describe high cycle fatigue damage and strain parameters to describe LCF damage. In high cycle fatigue, crack nucleation and extension at localized areas are a major damage mechanism, whereas the deformation of a whole part remains in elastic regime. Therefore, the microstructural change in high cycle fatigue is limited in the vicinity of a crack. In LCF, however, whole parts elasto-plastically deform nucleating many cracks in the early stage in fatigue process and some of them propagate to bring failure of machines and structures. Manson-Coffin law, where the damage parameter is written with strain, has been widely used but stress has an important role in LCF failure, especially nonproportional low cycle fatigue.

Additional hardening occurred under nonproportional loading, where principal axes change their directions with time. The additional hardening was reported to have a close connection with failure lives in nonproportional LCF, and

nonproportional parameters that introduce stress terms in combination with strain terms demonstrated that the additional hardening should be considered in estimating nonproportional LCF lives [1].

Some papers reported that the amount of the additional hardening is material dependent [2]. Certain FCC materials give large additional hardening resulting in a significant reduction in LCF lives but BCC materials little additional hardening resulting in apparent reduction in LCF lives [3]. The amount of additional hardening is material dependent even in FCC materials. The additional hardening is closely related with the microstructure development in the materials but the relationship is not well understood, whereas several studies have challenged this topic [2, 4-10].

The objective of this paper is to discuss the microstructure development in proportional and nonproportional loadings performed in the author's laboratory [2-4,7]. This paper firstly discusses the material dependence of the additional hardening by selecting five materials with a FCC crystallographic structure. The materials selected were Type 304 stainless steel (304SS), pure Cu, pure Ni, pure Al and 6061 Al. Tension-torsion proportional and nonproportional loading tests were performed and stress responses were experimentally obtained. The stress responses are discussed in relation with the stacking fault energy of the materials. The slip morphologies and dislocation structures are also discussed in relation with the stacking fault energy of the materials. Next, microstructures of specimens fatigued under 14 proportional and nonproportional loading paths are discussed in relation with the stress response on 304SS at room and high temperatures. Microstructures discussed are dislocation, cell, stacking fault and twin. Microstructure map is proposed to identify the boundary of cell formation.

### MATERIAL DEPENDENCE OF ADDITIONAL HARDENING

Five FCC materials with different stacking fault energies were cyclically loaded using proportional and nonproportional strain paths. The five materials and their stacking fault energies are tabulated in Tab. 1. All these materials have a FCC crystallographic structure. 304SS has the lowest stacking fault energy of 20 erg/cm<sup>2</sup>, pure Cu and pure Ni have intermediate stacking fault energies of 40 erg/cm<sup>2</sup> and 80 erg/cm<sup>2</sup>, respectively, and the two aluminums have the highest stacking fault energies of 200 erg/cm<sup>2</sup>.

Tension-torsion cyclic loading tests were performed using the hollow cylinder specimen of which the shape and dimensions are shown in Fig. 1 under the strain paths shown in Fig. 2, where  $\varepsilon$  is the axial strain and  $\gamma$  the shear strain. Tension loading was used as a proportional loading and alternating test between tension and torsion in every one cycle was used as a nonproportional test, Fig. 2 (a). Ten cycles with constant strain amplitude were repeated to obtain stable stress amplitude after the saturation of strain hardening. The stress amplitude at 10 th cycle in each block was recorded as representative one of the data. Mises strain amplitude of 0.05% was increased every 10 cycles, Fig. 2 (b).

SUS304	Pure Cu	Pure Ni	Pure Al	6061 Al
20	40	80	200	200

Table 1: Stacking fault energies  $\gamma$  (erg/cm<sup>2</sup>) of five FCC materials.

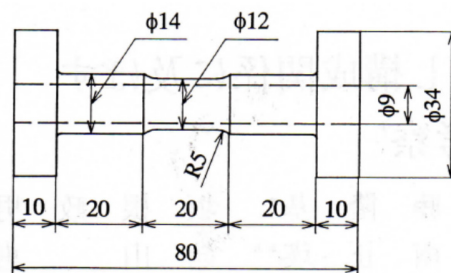


Figure 1: Shape and dimensions of specimen.

Fig. 3 shows cyclic stress-strain curves of the five materials. 304SS gives large additional hardening, Cu and Ni show intermediate additional hardening and Al and 6061 Al no additional hardening. Since no difference is found in the elastic part of the stress-strain curves in the figure, only the plastic part has the influence on the additional hardening. To quantify the relationship between the plastic strain amplitude ( $\varepsilon_p$ ) and stress amplitude ( $\sigma$ ), the following equation is introduced.



$$\sigma = A(\epsilon_p)^n \tag{1}$$

In the equation,  $A$  is the strain hardening coefficient and  $n$  the strain hardening exponent.

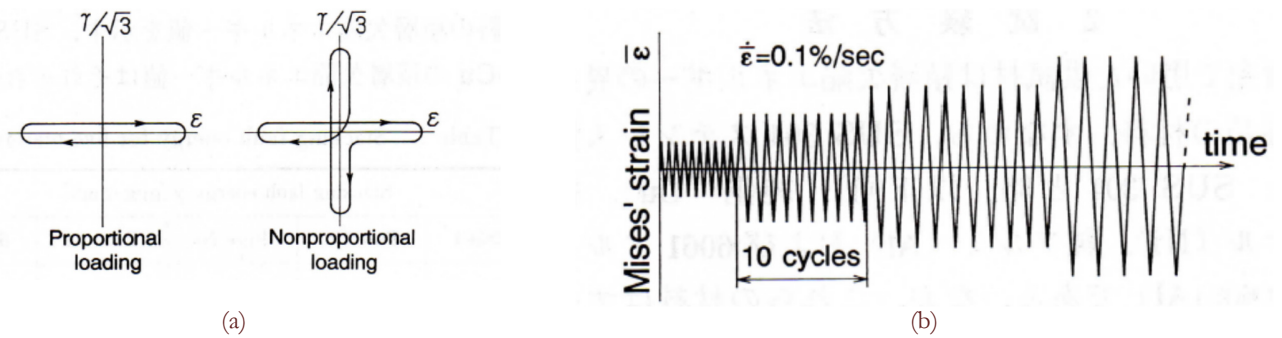


Figure 2: Strain path (a) and strain sequence (b).

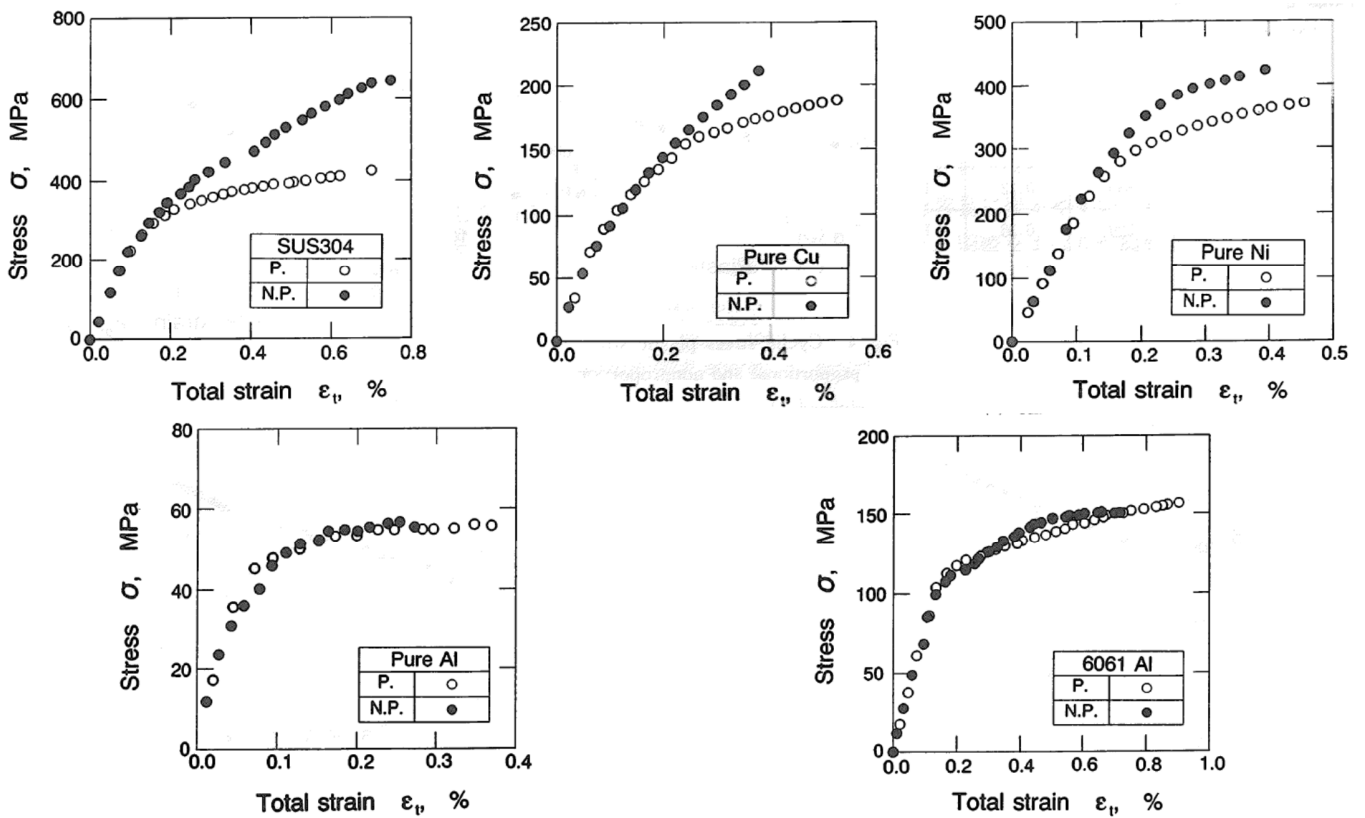


Figure 3: Cyclic stress-strain curves of five materials under proportional and nonproportional loadings.

Materials	Proportional		Nonproportional	
	$n_P$	$A_P(\text{MPa})$	$n_{NP}$	$A_{NP}(\text{MPa})$
SUS304	0.13	830	0.22	1860
Pure Ca	0.18	520	0.30	1330
Pure Ni	0.12	740	0.12	940
Pure Al	0.12	110	0.12	110
6061 Al	0.11	270	0.11	270

Table 2: Cyclic hardening coefficient and exponent.

Tab. 2 lists the strain hardening coefficient and exponent of the five materials and Fig. 4 relates the cyclic strain hardening coefficient and exponent ratios with the stacking fault energy, where the ratios are the coefficient and exponent in nonproportional loading divided by those in proportional loading. The two ratios both decreased with the stacking fault energy. The interesting characteristic in the figures is that there exist thresholds in the ratios. The cyclic hardening coefficient and exponent ratios start to increase at the stacking fault energy of around 80 erg/cm<sup>2</sup> and the additional hardening does not occur in the stacking fault energy range above about 80 erg/cm<sup>2</sup>.

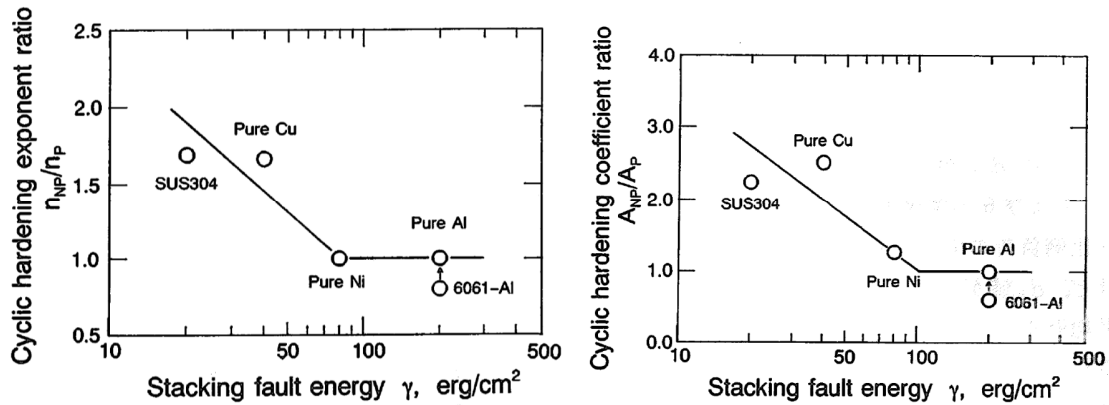


Figure 4: Relationship between strain hardening coefficient and exponent ratios and stacking fault energy.

The physical background of the large additional hardening in the materials with lower stacking fault energy is that a perfect dislocation in the materials is easy to split into two partial dislocations having a stacking fault between the two partial dislocations. The elastic strain energy of the two partial dislocations is lower than the perfect dislocation. The width of the stacking fault is larger in lower stacking fault energy material. Dislocations with large width of stacking fault are difficult to make cross slip to bypass obstacles like Lomer-Cottrell locks made by interactions of slip systems, because the partial dislocations have to shrink back to a perfect dislocation for making a cross slip. Therefore, the slip characteristics of the material with low stacking fault energy tends to be planar while that with high stacking fault energy to be wavy.

Fig. 5 shows SEM photographs observed on the replica films at the strain ranges shown in the figures. Unidirectional planar slip lines were observed on the photograph of 304SS in proportional loading, Fig. 5 (a), but slip lines in different directions in nonproportional loading were found, Fig. 5 (b). The maximum shear direction was fixed in proportional loading while the maximum shear direction changed in each cycle in nonproportional loading, which caused the different directional slips in 304SS in nonproportional loading. The similar slip characteristics, unidirectional slip lines in proportional loading and different directional slip lines in nonproportional loading, were found in Cu, Fig. 5 (c) and (d). No clear slip lines were found in Ni in proportional and nonproportional loadings and only the wavy surface appeared, Fig. 5 (e) and (f). Slightly curved slip lines were observed in Al in nonproportional loading but no clear slip lines were found in nonproportional loading, which was caused by the slips in many directions, Fig. 5 (g) and (h). No clear slip lines were found in 6061Al in proportional and nonproportional loadings, but the roughed surface along grain boundaries were found, Fig. 5 (i) and (j).

These results indicate that, in proportional loading, the unidirectional slip lines formed in the low stacking fault energy materials like 304SS and Cu but such clear unidirectional slip lines did not formed in the high stacking fault energy materials like Ni and 6061 Al. In nonproportional loading, slip lines in different directions were found in the low stacking fault energy materials like 304SS and Cu but such clear slip lines were not found in the high stacking fault energy materials like Ni, Al and 6061Al. Only the exception was Al in proportional loading, where clear slip lines formed. The slip lines in Al may have the possibility of being a brittle fracture of oxidation layer formed on the specimen surface.

Fig. 6 shows dislocation structures observed by TEM. Clear cells were found in all the tests. In 304SS and Cu, cell walls seem to have preferential orientations in proportional loading while they seem to be isotropic in nonproportional loading. The preferential orientation of cell walls may occur by the combination of the maximum shear stress direction and {111} crystallographic orientation. Isotropic cells were observed in Ni and Al and there was no clear difference in cell morphology between the proportional and nonproportional loadings. Especially, there were dislocations in the cells of Ni but no dislocations were found in the cells of Al.

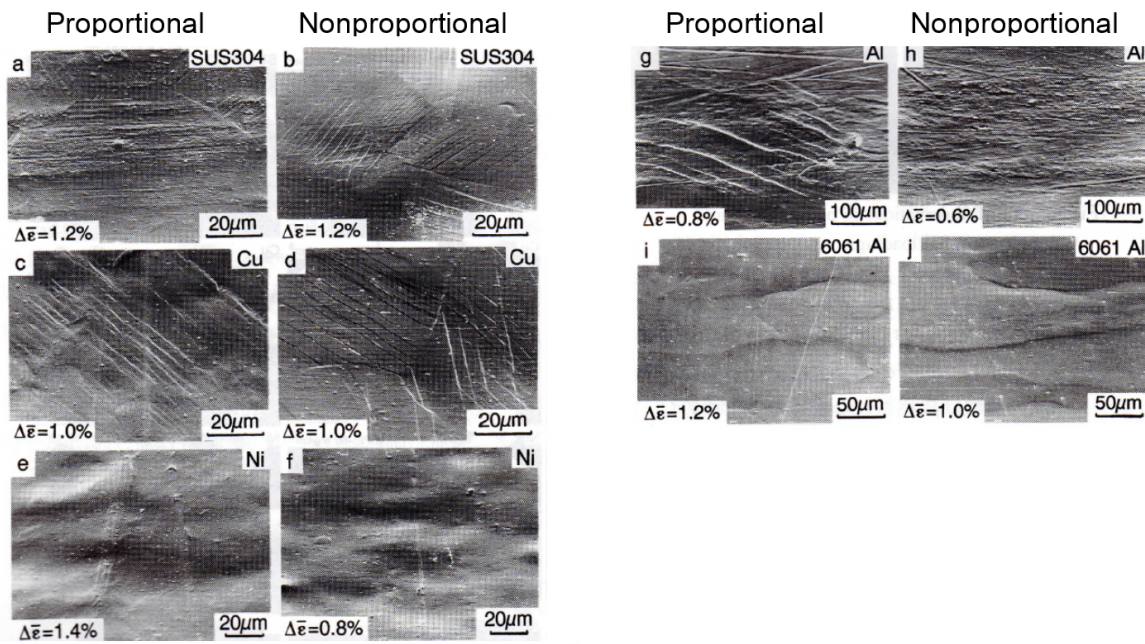


Figure 5: Slip lines observed on the specimen surface under proportional and nonproportional loadings.

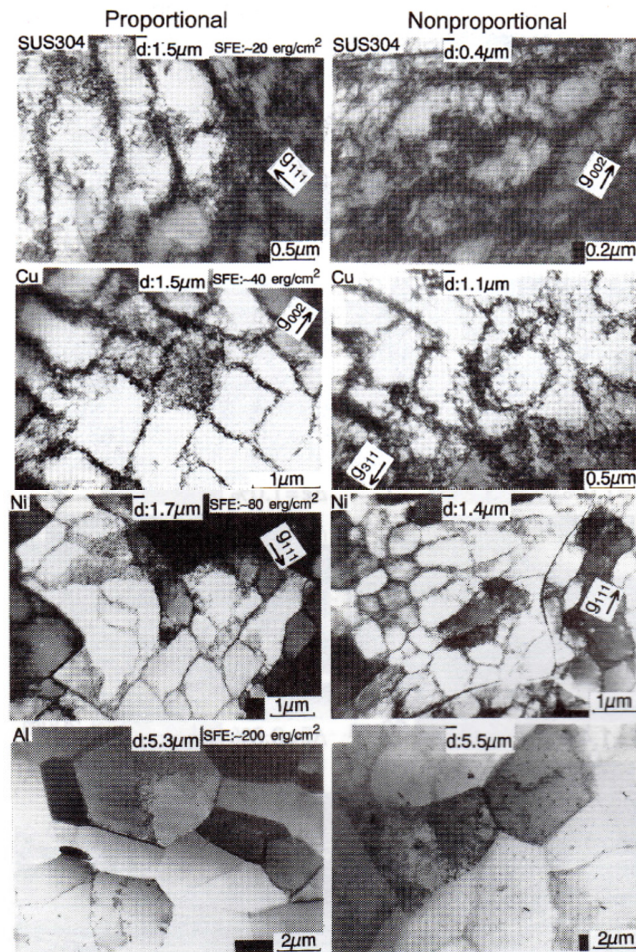


Figure 6: Dislocation structures observed by TEM.



Cell size has a close connection with the stress amplitude, so the stress ratio ( $\sigma_R$ ) and the square root of average cell diameter ( $\bar{d}_R$ ) is plotted in Fig. 7. The stress ratio is defined by the following equation to express the amount of the additional hardening of materials. The stress ratio represents the increase ratio caused by the additional hardening of each material. It is meaningless to take the stress increase by the additional hardening itself, because each material has different flow stress. So, this study employed the ratio shown in Eq. (2).

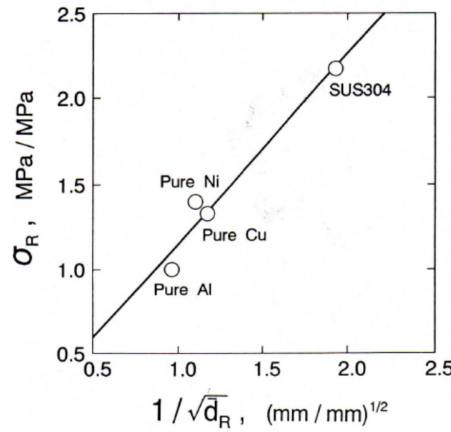


Figure 7: Stress ratio-mean cell size relationship.

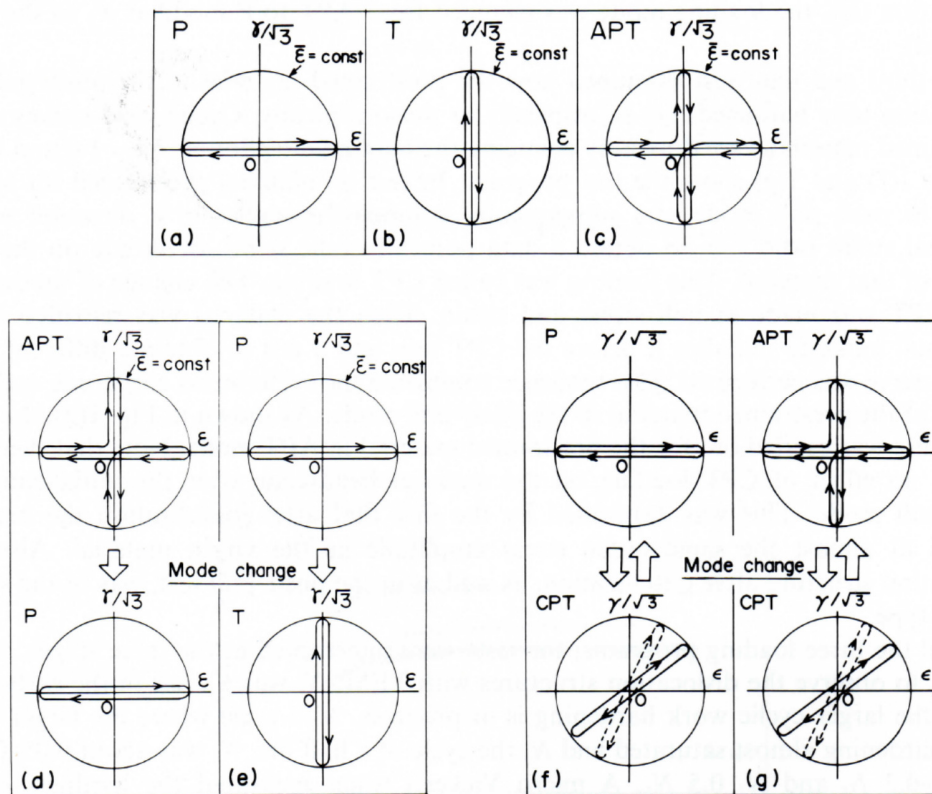


Figure 8: Strain paths and loading sequence.

$$\sigma_R = \frac{(\sigma_{mNP} - \sigma_{yp})}{(\sigma_{mp} - \sigma_{yp})} \quad (2)$$

$\sigma_{mNP}$  and  $\sigma_{mp}$  are the stress amplitude at the final cycle in the test in nonproportional and proportional loadings, respectively, and  $\sigma_{yp}$  is the yield stress in proportional loading. A linear relationship is found in the figure which indicates



that the stress increase observed in nonproportional loading mainly results from the reduction in the mean cell size, and the following Hall-Petch relationship holds.

$$\sigma_R = k \cdot \bar{d}_R^{-1/2} \tag{3}$$

The constant,  $k$ , takes the value of 1.2.

### MICROSTRUCTURE AND HARDENING BEHAVIOR OF TYPE 304 STAINLESS STEEL AT HIGH TEMPERATURE

Microstructure of 304SS was studied on the specimen after cyclically loaded at 823K using strain paths shown in Fig. 8. The chemical composition of the steel was 0.38 Si, 1.13Mn, 0.008P, 8.74Ni, 18.52Cr, 0.06C remainder Fe in weight percent ratio with ASTM No.3.5 grain size. In Fig. 8, (a) is the push-pull loading (P), (b) the reversed torsion loading (T) and (c) the alternating push-pull and reversed loading in each cycle (APT). Fig. 8 (d) is the strain path cyclically pre-strained in APT loading and switched to P loading, and Fig. 8 (e) is the strain path cyclically prestrained in P loading and switched to T loading. These (d) and (e) strain paths were motivated to study the re-arrangeability of the dislocation structure formed in the prestrain loading to that in the following loading. The (f) and (g) strain paths in Fig. 8 are the strain path to investigate the hardening characteristic of the material cyclically loaded in P and APT strain paths. The material was cyclically prestrained in P loading followed by many directional loadings in the figure to draw the hardening ellipse in (f), and (g) is the same loading path for the prestrained material in APT loading. Strain controlled tests were performed using the specimen geometry as shown in Fig. 1 with a triangular strain waveforms at 0.1Hz at 823K. Stress amplitudes in P, T and APT loadings at a Mises strain range of 1.0% are shown in Fig. 9. The P and T loadings, which are proportional strain path, give almost the same stress amplitude, but APT loading that is nonproportional strain path yields larger stress amplitude than P and T loadings. Clear cyclic strain hardening was observed in the three strain paths.

Fig. 10 shows dislocation structures at  $N_1$ ,  $N_2$  and  $N_3$  in the three loading paths at a Mises equivalent strain range of 1%, where  $N_1$  is the number of cycles where the cyclic work hardening almost saturated ( $\approx 0.05 - 0.1N_f$ ),  $N_2$  the number of cycles where rapid cyclic work hardening saturated ( $\approx 0.2 - 0.3N_f$ ) and  $N_3$  the life ratio of  $0.5N_f$ . Dislocation structures in P loading are mostly ladder, partly maze and less cells. APT loading yields only cell structure. The photographs in column  $N_1$  show that in all the loading modes dislocation structures form in the early stage of straining and that they are firmly established as cycling progresses.

Fig. 11 shows geometrical orientation of ladder and maze structures at  $N_3$ , where the equivalent strain range was 1.0%. Schematic figures on the right of Fig. 11 show  $\{111\}$  planes, i.e. the primary slip planes of the grains on which the maximum shear stress operates. They are distinguished from other slip planes according to the loading direction. Since the electron beam penetrates from the top to the bottom of the schematic figure, it is clear that the dense parts of ladder or maze structures are on  $\{111\}$  planes. This was also confirmed at  $N_1$  and  $N_2$ .

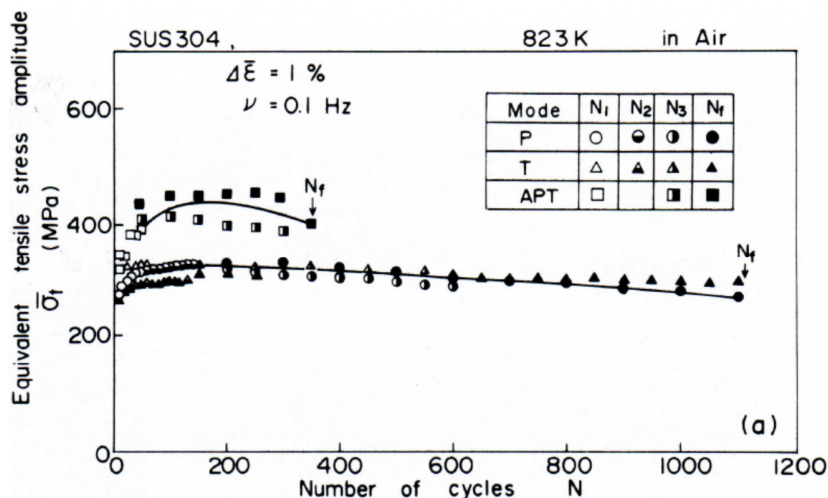


Figure 9: Stress amplitudes in P, T and APT loadings.

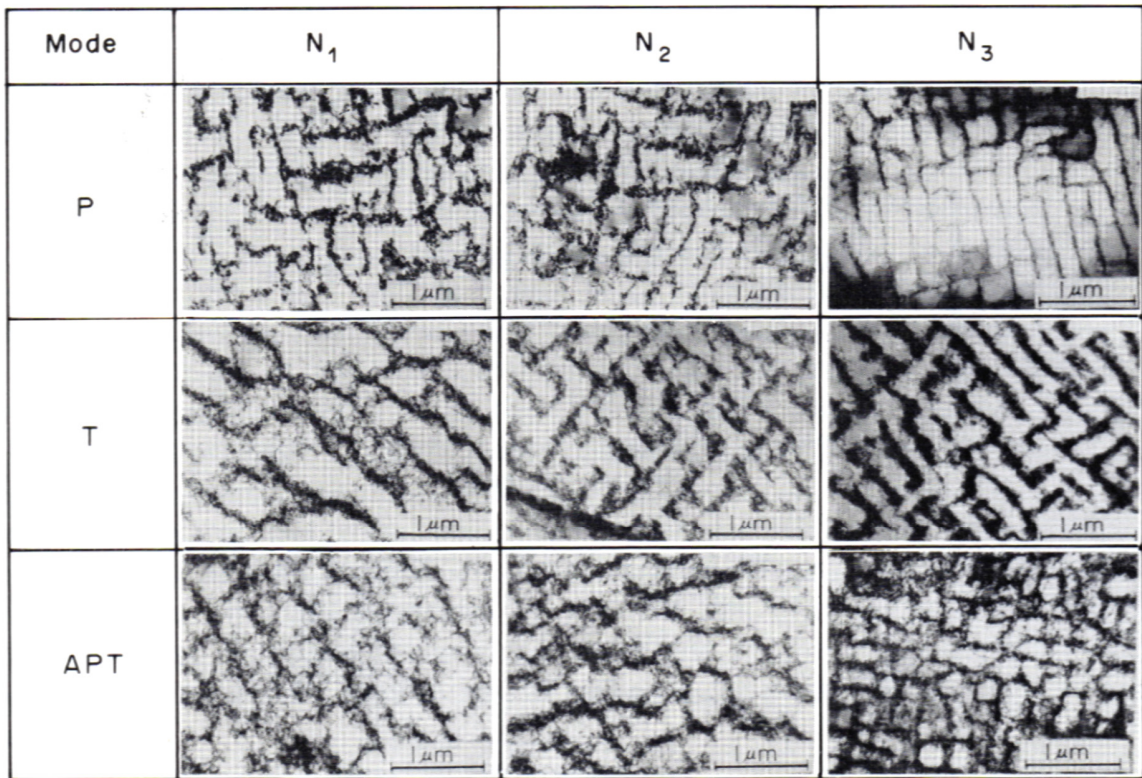


Figure 10: Dislocation structures in P, T and APT loadings.

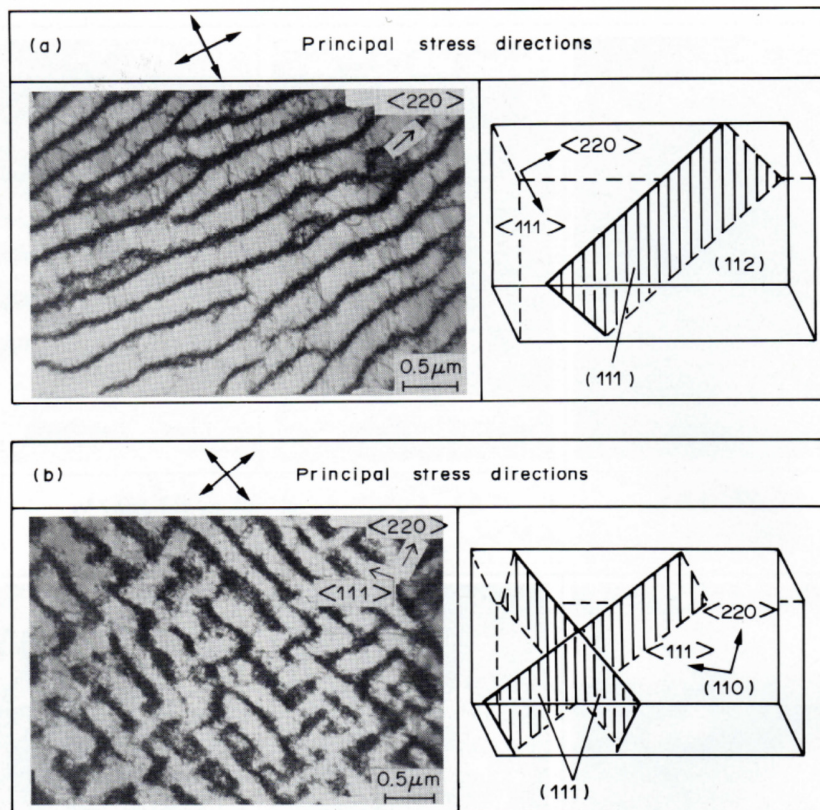


Figure 11: Dislocation structures in P and T loadings.

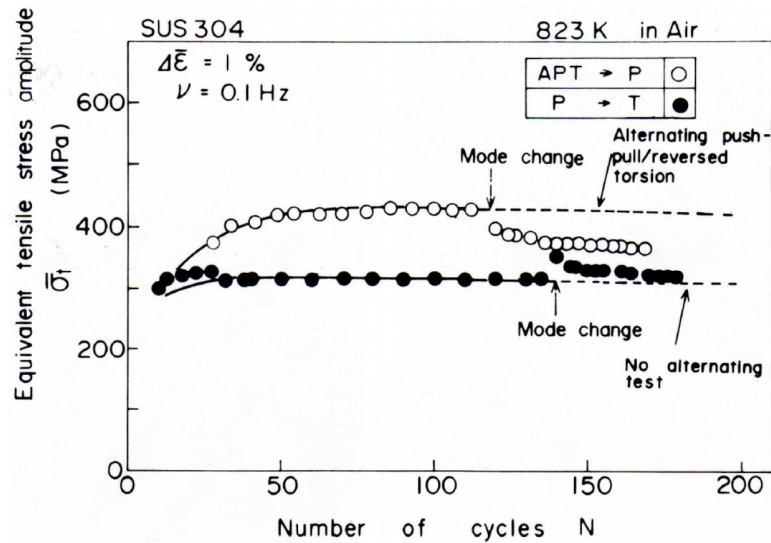


Figure 12: Variation of stress amplitude with cycles in loading mode change tests.

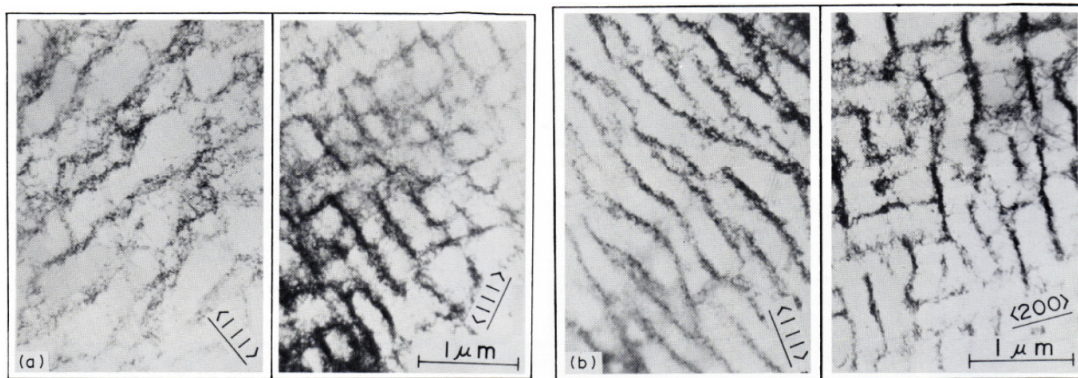


Figure 13: TEM observations for loading mode changes tests at 823K. (a) APT loading followed by P loading, (b) P loading followed by T loading.

Regarding the relationship between cyclic stress response and dislocation structure, the findings are as follows. In uniaxial LCF tests at room temperature, a cell structure is formed [2]. At elevated temperatures, however, ladder or maze structures form because of a thermally activated process which rearranges the dislocation structures into more ordered array having lower elastic strain energy. Mura et al. [11] reported that the maze and ladder structures have less strain energy than cell structure by the elastic calculation. In APT loading, on the other hand, the maximum shear strain changes the direction by 45 degrees in each cycle, so that larger interactions between the slip systems occur. In APT loading, the larger interactions result in a cell structure, because it prevents the rearrangement of the dislocations by the thermally activated process. The resistance to the dislocation glide is greater in the cell structure so that larger cyclic strain hardening results.

Fig. 12 shows the variation of stress amplitude with cycles in loading mode change tests from P to T and APT to P loadings. Looking at the loading mode change test from P to T, the stress amplitude jumped up in the cycle just switched to T loading, which is well known as the cross hardening effect. The stress amplitude gradually decreased with proceeding cycles after switching the loading mode and finally it reduced to the stress amplitude in the original P loading. This result indicates that once the cross hardening effect occurred by switching the loading mode but the effect disappeared by the following cyclic loading. We have to note that the experiments were performed at high temperature so that the thermal activation assisted the reduction in the stress amplitude after the switch. This result also implies that the microstructure was once disturbed by the switch of the loading mode but it was mostly reformed to the microstructure in the followed loading mode. The stress amplitude in APT loading before the switch was larger than that in P loading and it started to reduce after the switch of the loading mode to P. The stress amplitude after the switch did not reach to that in the original P loading and it stabilized at the higher stress amplitude than that in P loading. The reduction in the stress amplitude after



the switch resulted from the rearrangement of small cell structure formed in APT loading to the ladder structure by the cyclic loading with the assistance of the thermal activation but the small cell structure was too stable to rearrange completely. Only some parts of the cell structure developed in APT loading was rearranged to the microstructure in P loading.

Dislocation structures are shown in Fig. 13 after the loading mode change from APT to P in (a) and from P to T in (b). As seen in Fig. 13 (a), round shaped cell structure still remains, especially on the right side figure in (b), indicating the cell structure was not completely rearranged to that in P loading. The incomplete rearrangement of cell structure is the experimental background of the incomplete reduction in stress amplitude to P loading mode shown in Fig. 12. Clear ladder and maze cell structures were found in (b), which are the structures in P and T loadings. Especially, the maze structure is a specific cell structure in T loading, and these structures in (b) are the experimental background of the complete rearrangement of cell structure developed in prestraining and complete reduction in the stress amplitude after switching the loading mode.

Fig. 14 depicts the stress amplitude ellipse to express the hardening characteristics of the prestrained material in P and APT loadings at a Mises equivalent strain range of 1%. These data were obtained in the test that the material was cyclically strained to certain cycles to obtain the stable stress amplitude and was suddenly switched to the loading mode of combined tension and torsion to get a stress amplitude in Fig. 14. After measuring the stress amplitude, the loading was back to P loading to the cycle of stabilizing the stress amplitude and the loading mode again changed a different combination of combined tension and torsion to obtain a stress amplitude with another combination. The stress amplitude of the prestrained material in APT loading are collapsed on Mises line so the material was hardened isotropically. The isotropic hardening was also microstructurally confirmed from the round shaped cell structure shown in Fig. 10. Round cell structure has a same resistance in any directional loading. The stress amplitude of the prestrained material in P loading, on the other hand, showed anisotropic stress amplitude. The stress amplitudes of the prestrained material in P loading are rather on the line of  $\sigma^2 + 2\tau^2$ . The prestrained material in P loading had the ladder structure, and it showed the anisotropic resistance to preferential directions.

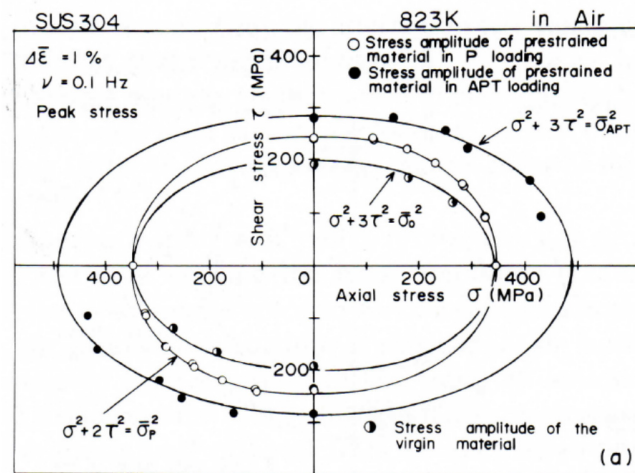


Figure 14: Stress amplitude ellipse for P and APT loaded materials.

## MICROSTRUCTURE IN VARIOUS STRAIN WAVEFORMS AT ROOM TEMPERATURE

Systematic multiaxial LCF tests were performed using 14 strain waveforms shown in Fig. 15 on 304 SS at room temperature. The figure represents the shear and axial strain applied to the tube specimen shown in Fig. 1 with a slight modification at gage part to avoid buckling and bulging under severe nonproportional loadings. Case 0 and Case 5 are a proportional loading and the other strain paths are all nonproportional loading. From the test results using the strain waveforms in the figure, various factors which influence multiaxial LCF lives are discussable but the detailed explanation of the factors is not presented here because this paper does not intend to discuss LCF lives in detail. Readers who are interested in how the factors are influential to nonproportional LCF lives can consult to the reference [12].

Fig. 16 illustrates the axial stress-shear stress hysteresis loops at two strain ranges in the respective strain paths. The shear stress-axial stress form the corresponding shapes with the strain waveforms and the stress range enlarged with the



nonproportionality of the strain path. Fig. 17 correlates the multiaxial LCF lives with the maximum principal stress, where numbers in the figure are the numbers of Cases. The figure clearly shows that all the multiaxial LCF lives are overestimated in the correlation with the maximum principal stress based on Case 0 lives. Considering that Mises strain and the maximum principal strain underestimated the nonproportional LCF lives, the stress or the strain only is not a suitable parameter for correlating multiaxial LCF lives but both the stress and strain should be taken into account. We have to note that only the stress or strain parameter is an approximation of the physical damage process in multiaxial LCF from the viewpoint of the simplicity for easy application of the parameter to designs of machines and structures.

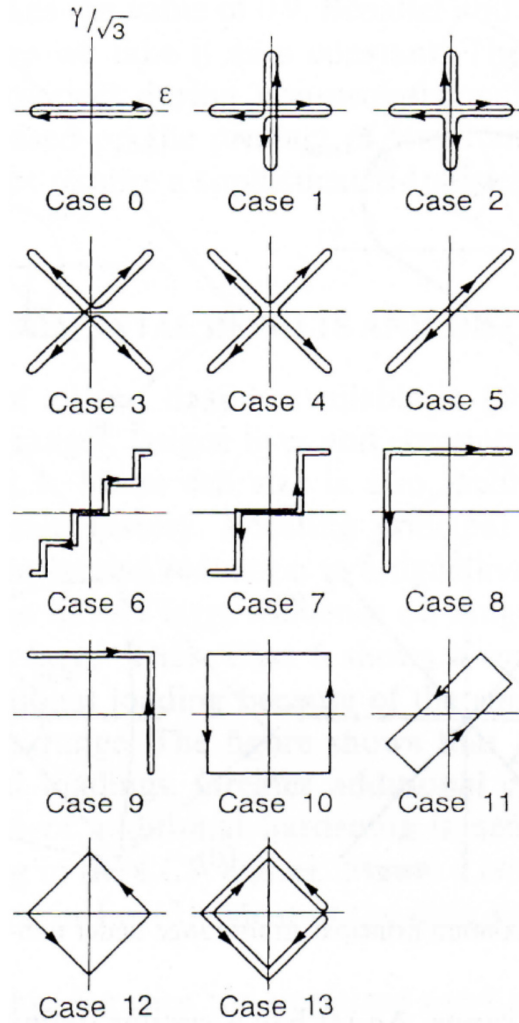


Figure 15: 14 strain waveforms used in LCF tests.

Fig. 18 (a)-(j) show the microstructure observed by TEM. Fig. 18 (a) shows the dislocation structure before testing where the dislocation density is very low and no specific substructure is identified. A cell structure is observed in Case 0, Fig. 18 (b), where the mean cell diameter is around  $1\mu\text{m}$ . Cell formation was also observed in the specimen cyclically loaded at large strain ranges ( $>1.0\%$ ) in Case 0. Dislocation bundles which indicate clusters of dislocations were observed at low strain ranges ( $<0.8\%$ ) in Case 0. Cell structures, twins and stacking faults were observed in Case 1, Fig. 18 (c), but only twins and stacking faults in Case 3, Fig. 18 (d). No clear cell formation was found in Case 3 and dislocation bundles were observed. Many stacking faults occurred before cell formation and they appear to hinder the cell formation in Case 3. The phasing of the applied strains produces larger stress and strain ranges for Case 3.

Nishino et al. [4] reported that a ladder or maze structure was a common structure for 304SS in proportional loading and a cell structure was primarily found in the nonproportional loading like Case 0 at high temperature as shown previously. At room temperature, however, cell structure formed and no ladder or maze structures were observed in Case 0. This difference of dislocation structure between room and elevated temperatures results from the difference in the thermal

activation. At elevated temperatures, dislocations glide more easily to form a structure with low elastic energy by the assistance of thermal activation so that a ladder or maze structure, which is a lower elastic energy microstructure than the cell, was found. In Case 5, which is a proportional straining, Fig. 18 (e), cell structures were observed. A deformation twin boundary was also observed at the center of the photograph. Diffraction pattern were taken for all the dislocation structures but it is difficult to distinguish between stacking fault and martensite that was observed by McDowell et al. [13].

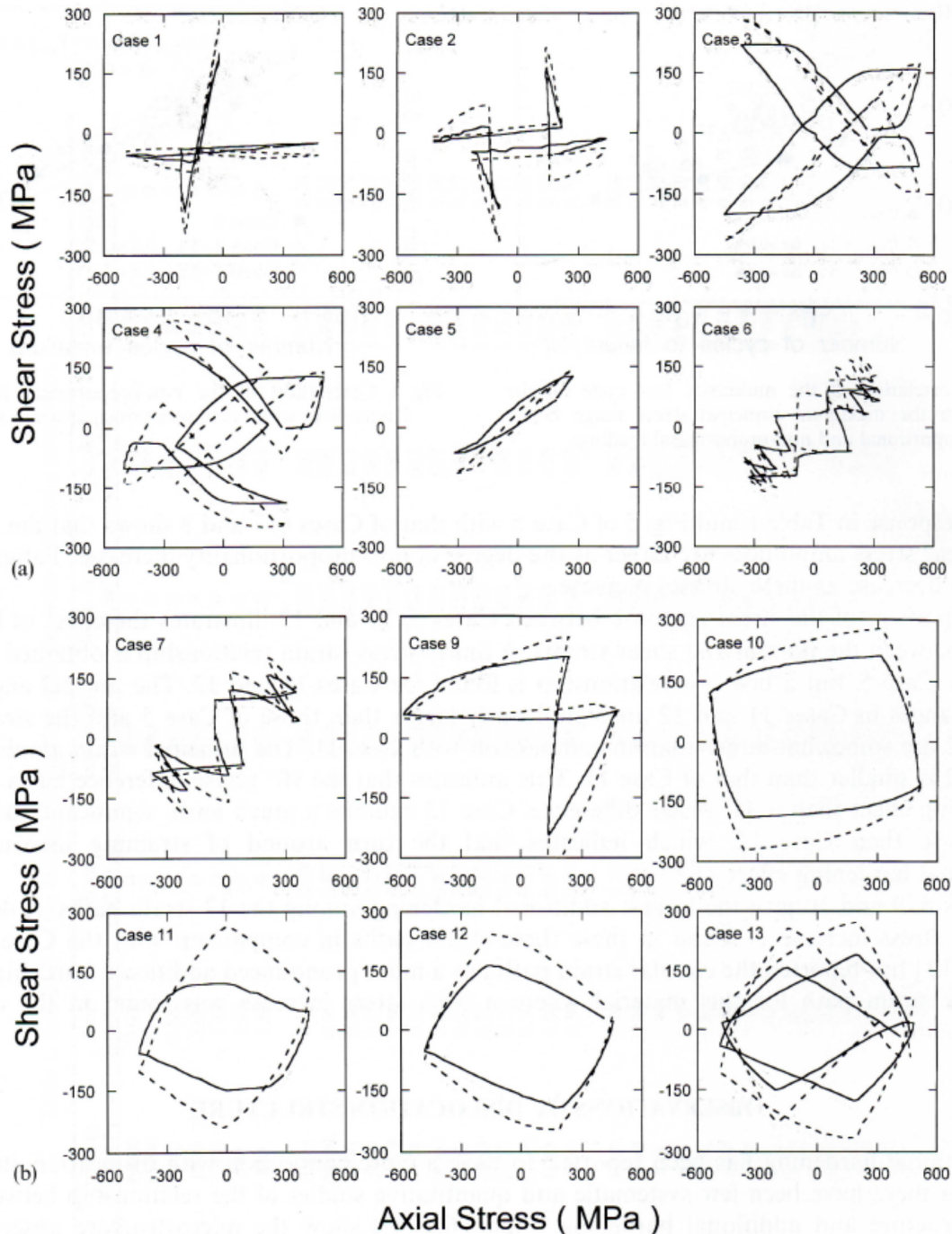


Figure 16: Shear stress-axial stress hysteresis loops under 14 strain waveforms.

Case 7, Fig. 18 (f), shows a coherent boundary of an annealing twin at the center of the photograph. Its role is similar to a grain boundary for the deformation microstructure. Dislocation walls are observed in the right of the photograph, and a cell structure is found in the left of the photograph. In Case 7, columnar cells were formed and Fig. 18 (f) shows the two



different sections of the columnar grains; the left is the normal section to columnar axes and the right is the parallel section of them. In Case 7, the maximum shear strain direction changed its direction, so that dislocations would easily rearranged to columnar structure by the cross slips.

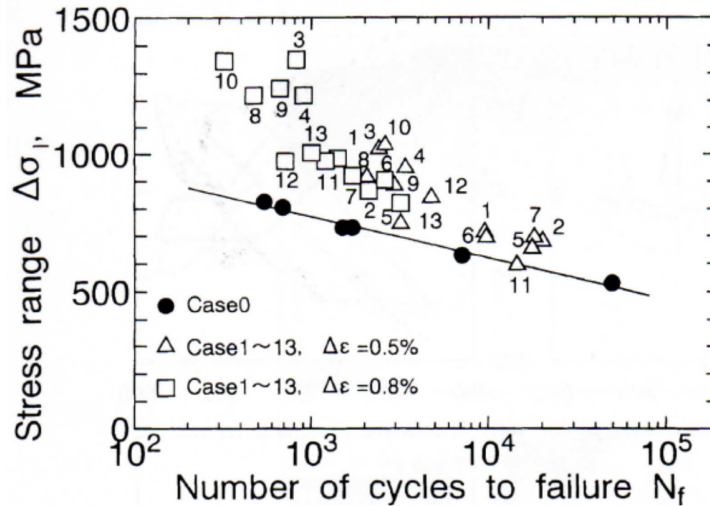


Figure 17: Correlation of multiaxial LCF lives with maximum principal stress.

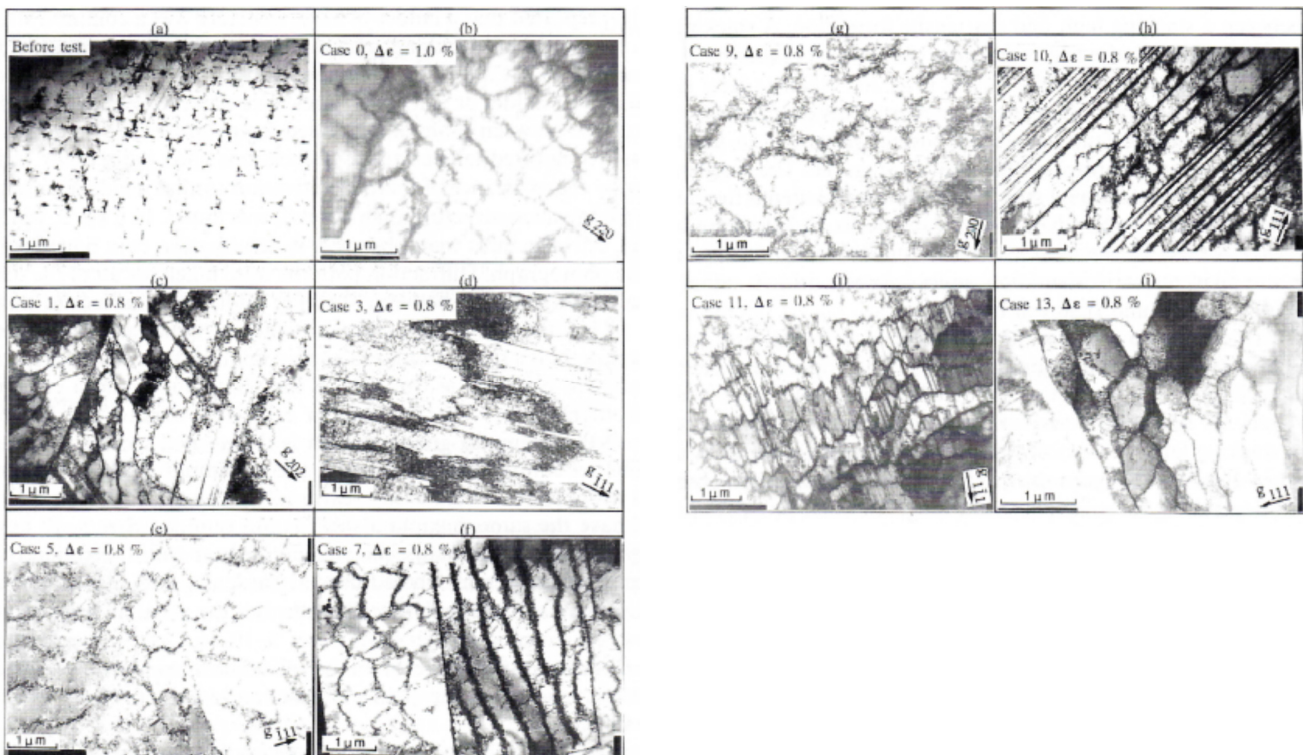


Figure 18: Microstructure observed TEM for typical loading paths.

Cases 5-10 all have the same maximum shear strain ranges. Cases 8-10 have a rectangular or box strain history. In these strain paths, the maximum shear strain direction rotates continuously, so that many slip systems operate. The additional hardening was most significant in these strain paths. Cases 11-13 are also rectangular strain paths but the phasing of the strain is such that the maximum shear strain range is smaller than Cases 5-10. In Case 9, Fig. 18 (g), cell boundaries are not clear, but many dislocations exist even in the cells. The maximum shear stress direction rotates continuously in Case 9, so many slip planes operate and interact, which results in the significant additional hardening.

In Cases 10 and 11, Fig. 18 (h) and (i), many stacking faults or martensite were observed. There is little difference between a stacking fault and martensite formation. A stacking fault forms when one atomic plane is dropped off and when more than two atomic planes have a disordering it is a different structure which may be martensite. Since 304SS is a material of low stacking fault energy, slip is planner as shown in Fig. 5 and there are many partial dislocations which make a stacking fault between them. Long stacking faults exceeding several subgrains in length were formed in Case 10 with short stacking faults formed within cells in Case 11. The long stacking faults were formed by the several box nonproportional straining and which hindered the cell formation, while, in Case 11, the cells were formed earlier than the stacking faults and stacking faults were stopped by the cell boundaries. For Case 13, fine cells are found and they are rather close to subgrain since the cell boundaries are rigid and misorientation angle between cells is rather large. This strain path made resulted in clear cells and rigid cell boundaries.

Fig. 19 is a microstructure map showing the cell, dislocation bundle and stacking fault boundaries as functions of maximum principal strain range and nonproportional factor for all the strain paths. In the figure, solid symbols indicate tests in which only cells were observed, while open symbols represent tests in which cells and other dislocation structures were found. Asterisks indicate tests where stacking faults were observed and the number at the data indicate the strain path number shown in Fig. 15. This figure shows that stacking faults were observed in almost all the tests and did not depend on the principal strain range and nonproportional factor. 304 SS is a low stacking fault material and a dislocation easily split into partial dislocations, making a stacking fault between them as discussed earlier. A partial dislocation glides on the slip plane, and a stacking fault arises between the partial dislocations. Many stacking faults seem to be generated by this mechanism. There is a critical combination of strain range and nonproportional factor for forming cells indicated by the solid line. In the region above the line, the microstructure is dominated by cells with other microstructure in addition to cells observed for the test conditions below the solid line.

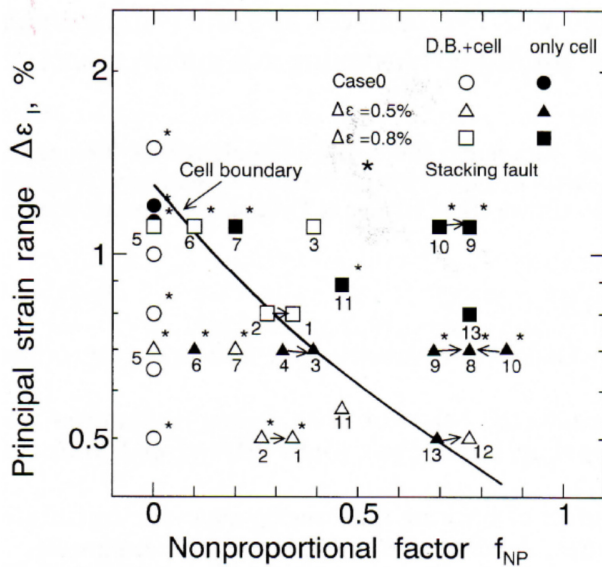


Figure 19: Microstructure map represented with principal strain and nonproportional factor.

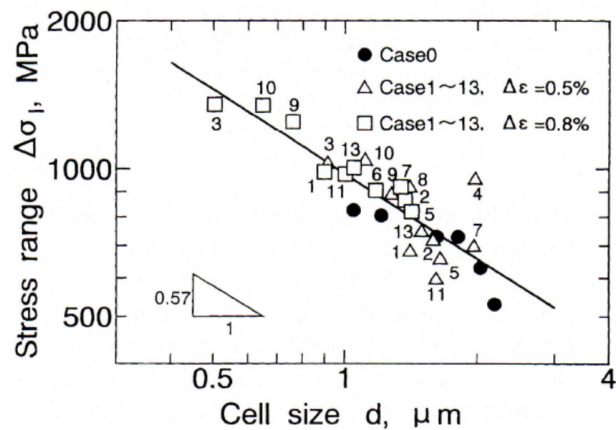


Figure 20: Relationship between principal stress range and cell size.

Fig. 20 shows the relationship between cell size and the maximum principal stress range for all the tests where the cell structure was observed. The mean cell size was determined by the Heyn method (JIS G005), observing 3 or 4 locations of each specimen. Maximum principal stress range ( $\Delta\sigma$ ) and mean cell size ( $d$ ) can be approximated by a straight line for all of the strain histories. The relationship is,

$$\Delta\sigma = m \times d^n \tag{4}$$

The values of  $m$  and  $n$  are 975MPa and  $-0.57$ , respectively when  $d$  is measured in  $\mu\text{m}$ . The value of exponent is close to  $-0.5$ , so that the Hall-Petch relationship holds in proportional and nonproportional loadings. As shown in Fig. 18, various microstructures were formed under nonproportional loading. However, the results in Fig. 20 indicate that the additional hardening in nonproportional loading is mainly caused by the reduction in cell size. The severe interaction of

slip systems under nonproportional loading reduces the cell size and results in the additional hardening. The results also imply that microstructures other than cell structure have almost no influence on the additional hardening.

### MICROSTRUCTURE IN VARIOUS STRAIN WAVEFORMS AT HIGH TEMPERATURE

Microstructures of 304 SS were also studied at 923K on the specimen fatigued using 14 strain paths shown in Fig. 15. The TEM photographs are not presented here but the same microstructure map as Fig. 19 is shown in Fig. 21, where the results at room temperature are also shown by the dashed line. The figure clearly shows that the cell boundary at 923K shifted downwards from that at room temperature. The low positioned boundary indicates that cells were easily formed by lower principal stress and lower nonproportional factor at high temperature than at room temperature, which results from the activated mobility of dislocations at high temperature.

The relationship between the principal stress range and the cell size at 923 K is shown in Fig. 22, where the results at room temperature are superimposed in the figure. The same principal stress range at 923K formed smaller cell size by about 4 times compared with room temperature. The smaller cell size results from the activated mobility of dislocations at high temperature. The cell structure is a structure with lower elastic energy than the dislocation bundle and dispersed dislocations.

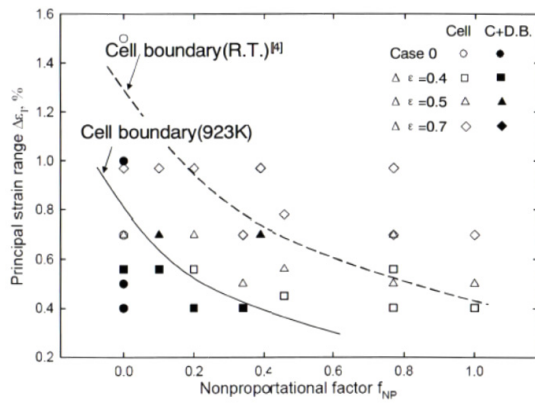


Figure 21: Microstructure map represented with principal strain range and nonproportional factor.

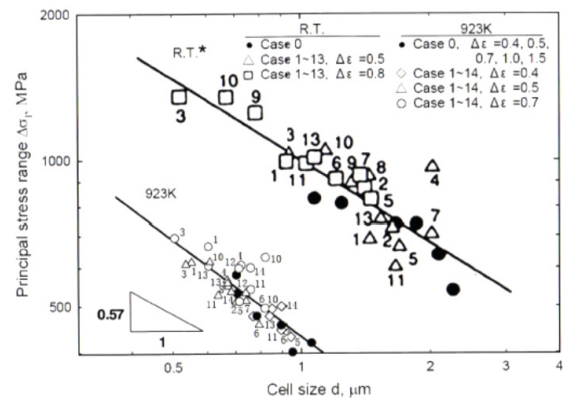


Figure 22: Relationship between principal strain range and cell size.

### CONCLUSIONS

1. FCC materials with low stacking fault energy showed large additional hardening but those with high stacking fault energy little additional hardening. The amount of the additional hardening results from the slip system of material. Materials with low stacking fault energy yielded planar slips and severe interactions of the slip systems caused large additional hardening. Those with high stacking fault energy gave wavy slips and a little interactions of the slip systems caused little additional hardening. The planar slip was caused by a perfect dislocation splitting into two partial dislocations and cross slip of the dislocation was difficult because two partial dislocations should shrink back to a perfect dislocation to make cross slip.
2. Ladder and maze structures were developed in 304SS cyclically loaded in tension and torsion at 923K. The microstructures were an anisotropic microstructure and the structures showed cross hardening. These microstructures were easily rearranged to another microstructure by switching the loading mode. Only a cell structure was formed in cruciform loading path and the cell structure was not completely rearranged by changing the loading mode. The small cell structure showed isotropic stress response. The amount of the additional hardening was caused by the reduction in cell size.
3. Stacking fault, cell, twin and dislocation bundles were observed in 304SS cyclically loaded under 14 proportional and nonproportional strain paths at room temperature. There was a critical boundary of the cell formation in a diagram presented with principal strain range and nonproportional factor. Hall-Petch relationship held between the principal stress range and mean cell size, indicating the additional hardening mainly resulted from the reduction in cell size.



4. Stacking fault, cell, twin and dislocation bundles were observed in 304SS cyclically loaded under 14 proportional and nonproportional strain paths at 823 K as well as at room temperature. The similar critical boundary was also found at 823K but the boundary was shifted downwards at 823K, compared with room temperature. Hall-Petch relationship also held at 823K but the cell size was four times smaller to yield the same principal stress range than at room temperature.

## REFERENCES

- [1] Socie, D., Marquis, G., *Multiaxial Fatigue*, Society of Automotive Engineers, Inc., Philadelphia, (2000).
- [2] Itoh, T., Sakane, M., Ohnami, M., Ameyama, K., Effect of Stacking Fault Energy on Cyclic Constitutive Relation under Nonproportional Loading, *J. Soc. Materials Science, Japan*, 41(1992) 1361-1367.
- [3] Itoh, T., Yang, T., Material Dependence of Multiaxial Low Cycle Fatigue Lives under Non-proportional Loading, *International J. Fatigue*, 33(2011) 1025-1031.
- [4] Nishino, S., Hamada, N., Sakane, M., Ohnami, M., Matsumura, N., Tokizane, M., Microstructural Study of Cyclic Strain Hardening Behavior in Biaxial Stress States at Elevated Temperature, *Fatigue Fract. Eng. Mater. Struct.*, 9(1986) 65-77.
- [5] Doong, SH., Dislocation Substructures and Nonproportional Hardening, *Trans. ASME, JEMT*, 112 (1990) 456-464.
- [6] Clavel, M., Feugas, X., Micromechanisms of Plasticity under Multiaxial Cyclic Loading, *Multiaxial Fatigue and Design, ESIS 21*, Mechanical Engineering Publication, (1996) 21-41.
- [7] Kida, S., Itoh, T., Sakane, M., Ohnami, M., Socie, D., Dislocation Structure and Non-Proportional Hardening of Type 304 Stainless Steel, *Fatigue Fract. Eng. Mater. Struct.*, 20(1997) 1375-1386.
- [8] Xiao, Lin., Umakoshi, T., Sun, J., Biaxial Low Cycle Fatigue Properties and Dislocation Substructures of Zircaloy-4 under In-phase and Out-of-phase Loading, *Materials Science and Engineering, A292(2000)* 40-48.
- [9] Xiaoshan, L., Guoqiu, H., Xiangqun, D., Defeng, M. Weihua Z., Fatigue Behavior and Dislocation Substructure for 6063 Aluminum Alloy under Nonproportional Loadings, *International J. Fatigue*, 31(2009) 1190-1195.
- [10] Dong, Y., Kang, G., Liu, Y., Wang, H., Chan, X., Dislocation Evolution in 316L Stainless during Multiaxial Ratchetting Deformation, *Materials Characterization*, 65(2012) 62-72.
- [11] Mura T., Shirai, H., Weertman, J. R., The Elastic Energy of Dislocation Structure in Fatigued Metals, *Proc. 2nd Inter. Symp. And 7th Canadian Fracture Conference on Defects, Fracture and Fatigue*, (1982) 67-74.
- [12] Itoh, T., Sakane, M., Ohnami, M., Socie, D., Nonproportional Low Cycle Fatigue Criterion for Type 304 Stainless Steel, *Trans. ASME, JEMT*, 117(1995) 285-292.
- [13] McDowell, D., Stahl, D., Stock, S., Antolovich, S., Biaxial Path Dependence of Deformation Substructure of Type 304 Stainless Steel, *Metallurgical Trans. A* 19A(1988) 1277-1293.